Available online at www.sciencedirect.com
ScienceDirect
Icarus 186 (2007) 97–110
ICARUS
www.elsevier.com/locate/icarus

Winter polar warmings and the meridional transport on Mars simulated with a general circulation model

Alexander S. Medvedev *, Paul Hartogh

Max Planck Institute for Solar System Research, Max-Planck-Str. 2, Katlenburg-Lindau, D-37191, Germany

Received 16 January 2006; revised 24 July 2006

Available online 24 October 2006

Abstract

Winter polar warmings in the middle atmosphere of Mars occur due to the adiabatic heating associated with the downward branch of the cross-equatorial meridional circulation. Thus, they are the manifestation of the global meridional transport rather than of local radiative effects. We report on a series of numerical experiments with a recently developed general circulation model of the martian atmosphere to examine the relative roles of the mechanical and thermal forcing in the meridional transport. The experiments were focused on answering the question of whether the martian circulation is consistent with the thermally driven nearly inviscid Hadley cell, as was pointed out by some previous studies, or it is forced mainly by zonally asymmetric eddies. It is demonstrated that, under realistic conditions in the middle atmosphere, the meridional transport is maintained primarily by dissipating large-scale planetary waves and solar tides. This mechanism is similar to the "extratropical pump" in the middle atmosphere on Earth. Only in the run with artificially weak zonal disturbances, was the circulation reminiscent of thermally induced Hadley cells. In the experiment with an imposed dust storm, the modified atmospheric refraction changes the vertical propagation of the eddies. As the result, the Eliassen–Palm fluxes convergence increases in high winter latitudes of the middle atmosphere, the meridional transport gets stronger, and the polar temperature rises. Additional numerical experiments demonstrated that insufficient model resolution, increased numerical dissipation, and, especially, neglect of non-LTE effects for the 15 μm CO_2 band could weaken the meridional transport and the magnitude of polar warmings in GCMs.

Keywords: Atmospheres, dynamics; Mars, atmosphere; Meteorology

1. Introduction

Temperature inversions and the related warmings in the martian middle atmosphere over the winter poles are the persistent features, which have been observed during both northern (e.g., Theodore et al., 1993; Santee and Crisp, 1993) and southern winters (e.g., Deming et al., 1986). They usually occur between 50 and 80 km, have magnitudes from several to tens Kelvin degrees, and, apparently, are stronger during northern winter solstices. Rothermel et al. (1988) reported on the winter polar mesosphere $\sim 70 \pm 20$ K warmer compared to the equatorial region. Some observations (Jakosky and Martin, 1987) point out to a coincidence between the onset of dust storms and the temperature increase over the winter pole. It was recognized (e.g., Barnes and Haberle, 1996; Wilson, 1997, and references therein) that these polar warmings have a dynamical rather than a radiative nature, and are related to the adiabatic heating due to the descending branch of the transport circulation over the winter pole. Thus, the polar warmings are not local phenomena but the manifestation of the global meridional transport on Mars.

Earlier numerical experiments with martian general circulation models (GCMs) failed to reproduce strong temperature increases over the winter poles. In part, this inability was explained by insufficiently high upper lids of the model domains, which prevented a full development of the Hadley circulation (Barnes and Haberle, 1996). Later, it was shown that a strong northern winter polar warming can be simulated with an increased amount of dust approximately corresponding to dust storm conditions. Wilson (1997) demonstrated that the aerosol heating expands the Hadley circulation poleward, and results in

* Corresponding author. Fax: +49 (0) 5556 979 240.
E-mail addresses: medvedev@mps.mpg.de (A.S. Medvedev), paul@mps.mpg.de (P. Hartogh).

0019-1035/$ – see front matter
doi:10.1016/j.icarus.2006.08.020

stronger downward motions over the pole. Further GCM simulations (e.g., Forget et al., 1999; Moudden and McConnell, 2005) corroborated the finding that a high dust opacity in numerical models leads to stronger polar warmings. Note, however, that the local radiative effect of aerosol is too small in high winter latitudes to be alone responsible for the temperature increase.

The origin of the quasi-global solstitial circulation in the atmosphere of Mars has often been attributed primarily to the latitudinal temperature gradient (Wilson, 1997; Forget et al., 1999). The resulting transport is then associated with the well-known almost inviscid Hadley circulation with its thermally direct cells: rising and sinking air induced by the differential heating, the poleward flow due to the conservation of mass, and the return flow near the surface (trade winds). This kind of transport cells is observed in the terrestrial troposphere over the tropics. It can be understood as a non-linear axisymmetric circulation driven by the latitudinal thermal gradient (Schneider, 2006, and references therein). In a less idealized case, the diffusivity and non-axisymmetric eddies (waves) significantly affect the Hadley circulation. It has been argued (Wilson, 1997; Forget et al., 1999) that on Mars, the circulation of this kind may extend higher and across the globe due to the pole-to-pole thermal contrast, unlike on Earth, where the Hadley cell is confined to tropics.

Despite the temptation to interpret the meridional transport (and the related polar warmings) entirely in terms of the thermally driven Hadley circulation, one important factor should be considered. The middle atmosphere of Mars over the winter poles is far from the radiative equilibrium, much unlike the thermal structure below. This implies an existence of a dynamical forcing which maintains the departure of the temperature from its radiative equilibrium values. The global atmospheric circulation on Mars is similar to the one on Earth in the sense that the pole-to-pole solstitial cell is also strong in the terrestrial middle atmosphere. The temperature maxima over the winter poles are also present on Earth during both solstices. They form winter polar extensions of the stratopause, and thus are partially obscured by the latter. The cross-equatorial transport in the terrestrial stratosphere is induced primarily by breaking planetary waves, while gravity waves and tides are the effective drivers of the circulation in the mesosphere (Andrews et al., 1987). This so-called "extratropical pump" mechanism (e.g., Holton et al., 1995) can play a role on Mars as well. Barnes (1990) and Collins et al. (1997) studied the possible role of breaking gravity waves on the martian middle atmosphere. Employing a GCM, Barnes and Hollingsworth (1987) explored the potential causation of sudden polar warmings by planetary waves. Hartogh et al. (2005) noticed a strong sensitivity of the polar temperature to the variations in the large-scale eddy forcing. Using GCM simulations, they demonstrated that the meridional circulation is driven primarily by eddies during both solstices (aerocentric longitudes $L_s = 90°$ and 270°), at least below 70 km and outside the tropics. In particular, it was shown that a strong southern polar warming can be simulated without increase in the dust load.

In this paper, we apply our newly developed martian GCM (Hartogh et al., 2005) to examine the effects of the mechanical (eddy) and diabatic (radiative) forcing on the meridional circulation and the associated winter polar warmings. Given the paucity of measurements above 50–60 km, GCM experiments provide insight on the nature of the circulation in the middle atmosphere of Mars: whether it primarily is induced thermally by the differential heating (Hadley cell), or driven mechanically by breaking/dissipating waves ("extratropical pump"), as on Earth. The martian GCM is briefly described in Section 2. The results of simulations are given in Section 3, and discussed in Section 4. Further numerical tests showing the sensitivity of the simulated warmings to GCM parameters are presented in Section 5.

2. Model description

The recently developed general circulation model of the martian atmosphere was described in detail by Hartogh et al. (2005). It represents a deeply re-designed version of the Cologne Model of the Middle Atmosphere (COMMA), a terrestrial GCM used for studies of the Middle atmosphere dynamics and photochemistry (e.g., Berger and von Zahn, 1999; Hartogh et al., 2004). A brief description of the martian GCM is given below.

2.1. Dynamics

The dynamical core of the model is the finite-difference (grid point) solver for the primitive equations of the hydrodynamics under the hydrostatic approximation on a sphere. The equations for the horizontal momentum, the thermodynamic and the continuity equations are discretized on a regular grid. The horizontal resolution used in this study is 32 × 36 grid points in the longitude and latitude, respectively. The model employs the log-pressure vertical coordinates $z = -H \log(\rho_0/\rho_s)$, where ρ_0 is the background density profile, ρ_s is the reference density at some height; $H = RT_s/g = 10.3$ km is the scale height, T_s is the constant reference temperature, R is the gas constant; g is the acceleration of gravity. We use 100 vertical levels, which span the atmosphere from the surface to approximately 10^{-4} mb (or 113 log-pressure km) with $\Delta z \approx 1.2$ km resolution. The topography is prescribed from the Mars digital elevation model derived from the Mars Orbiter Laser Altimeter (MOLA) profiles (Delacourt et al., 2003).

The model utilizes the centered ("leapfrog") time-differencing scheme with the Asselin time filter. The time step was set to 100 s. A "near pole" Fourier filter is applied to the simulated prognostic fields at latitudes higher than 82.5° (Takacs and Balgovind, 1983). It truncates all zonal harmonics higher than 2 to maintain the stability of the model without decreasing the time step. To prevent a build-up of the energy at the shortest resolved spatial scales and the associated instability, a horizontal dissipation is introduced in the form of the Shapiro (1970) filter.

2.2. Radiation

The model takes into account the radiative transfer in the gaseous CO_2 15 μm band, the CO_2 near-infrared bands, as well as the radiative effects of the mineral dust in the entire spectrum from 0.1 to 200 μm except for wavelengths coinciding with the CO_2 15 μm band.

For the CO_2 15 μm band in the upper atmosphere, we use an optimized version of the exact non-LTE ALI–ARMS (Accelerated Lambda Iteration for Atmospheric Radiation and Molecular Spectra) code described by Kutepov et al. (1998) and Gusev and Kutepov (2003). The code utilizes a differential equation approach to solve the radiative transfer equation, and relies on the exact accelerated lambda iteration (ALI) solution (Rybicki and Hummer, 1992). The opacity distribution function (ODF) technique (Mihalas, 1978) together with the reduced number of the CO_2 vibrational levels and bands help to accelerate the calculations. The solution accounts for the breakdown of the local thermodynamic equilibrium (non-LTE) in the middle atmosphere as well as for the radiative properties of the surface. In our simulations, we use the surface albedo map (Christensen et al., 2001) obtained from the TES observations. Note that the calculations of the cooling/heating rates due to the CO_2 15 μm band are performed every 1200 s, i.e., once for every 12 time steps in the dynamics.

Compared to Hartogh et al. (2005), a LTE radiation scheme of Nakajima et al. (2000) is now used in the model for the CO_2 15 μm band in the lower atmosphere. This scheme is based on the k-distribution method, and was originally developed for terrestrial climate models. Subsequently, it has been adapted for martian GCMs (Kuroda et al., 2005). The cooling rates computed with the non-LTE scheme of Kutepov et al. (1998) and with the LTE scheme of Nakajima et al. (2000) are smoothly merged near 40 km, where both algorithms give virtually identical values.

Heating rates due to the absorption of the solar radiation in the CO_2 near-infrared bands are computed using the parametric formula from Forget et al. (1999). This parameterization accounts for non-LTE conditions in the middle atmosphere. Some comparison of the resulting heating rates with the detailed line-by-line calculations is given in Hartogh et al. (2005).

The absorption, emission and scattering by the atmospheric dust are calculated by the two-stream discrete-ordinate/adding method (Nakajima and Tanaka, 1986). The dust parameters, refractive indices and particle size distribution are essentially the same as described in Hartogh et al. (2005). The major update in the current version of the model is the use of 19 representative wavelength bands instead of 4: 9 in the visible and 10 in the infrared. The nominal dust scenario for $L_s = 90°$ includes a horizontally uniform distribution of dust with the infrared optical depth 0.05 (scaled to an equivalent 7 mb pressure level). This value is in agreement with estimations of Liu et al. (2003, Fig. 10), and somewhat lower than in the retrievals of Smith (2004) ($0.05 < \tau < 0.1$ from Fig. 7). The visible optical depth rather than the one in IR is commonly employed in many martian GCMs. With the chosen set of dust parameters, $\tau = 0.05$ in IR corresponds to 0.18 in the visible. The vertical dust mixing ratio, Q, is given by the function

$$Q = Q_0 \exp\left\{0.007\left[1 - \left(\frac{p_0}{p}\right)^{70/z_{\max}}\right]\right\}, \tag{1}$$

where $z_{\max}$ depends on a latitude ϕ. At $L_s = 90°$, it is prescribed as

$$z_{\max}(\phi) = 50 - 11\sin^2\phi \text{ [km]}. \tag{2}$$

2.3. Vertical turbulent mixing

The model utilizes a standard turbulent diffusion parameterization for the free atmosphere based on the Richardson number. The parameters were adapted from the terrestrial NCAR-CAM3 (National Center for Atmospheric Research—Community Atmospheric Model) GCM (Holtslag and Boville, 1993). The atmospheric diffusivities for the momentum, K_u, and temperature, K_T, are taken as functions of length scales l_c and local vertical gradients of the wind and virtual potential temperature

$$K_c = l_c^2 S F_c(Ri), \tag{3}$$

where S is the local wind shear, the vertical mixing length is set to 30 m, and the stability functions $F_c(Ri)$ give the dependence on the local Richardson number Ri. For the simplicity, no distinction is made between the diffusivity coefficients for the wind and temperature, $K_u = K_T = K_c$. The following stability functions are employed in the model (Holtslag and Boville, 1993):

$$F_c(Ri) = (1 - 18Ri)^{1/2}, \quad Ri < 0,$$
$$F_c(Ri) = \left[1 + 10Ri(1 + 8Ri)\right]^{-1}, \quad Ri \geqslant 0. \tag{4}$$

2.4. Gravity wave drag

The impact of subgrid-scale gravity waves is parameterized using the spectral scheme of Medvedev and Klaassen (2000) adapted to orographically generated harmonics with zero phase velocities. The source magnitudes of gravity waves just above the resolved topography are estimated after McFarlane (1987) using the subgrid-scale variance of the elevations. The latter has been calculated from the high resolution topography map (Delacourt et al., 2003). The direction of the gravity wave propagation is chosen along the mean wind at the source level. The scheme uses no other tunable parameters except for the characteristic horizontal wavelength of the harmonics. In our simulations it is taken as 200 km, the middle value between the typical wavelengths 100 and 300 km employed in terrestrial GCMs of the comparable horizontal resolution (Medvedev and Klaassen, 2000).

2.5. Convective adjustment and Rayleigh friction

The turbulent diffusion parameterization reacts on the convectively unstable temperature profiles by the enhanced thermodiffusion coefficients. As with other GCMs, this diffusion

cannot alone describe processes of rapid mixing within the unstable layers. We employ a standard energy-conserving convective adjustment scheme to prevent superadiabatic lapse rates in the numerical solution completely. In the model, it is called after the turbulent diffusion scheme to restore the stability of the atmosphere by adjusting the temperature in the vertical column and keeping the potential temperature gradients positive.

Rayleigh friction is imposed near the top of the model. It imitates the missing damping effects in the upper atmosphere, and serves to reduce a numerical wave reflection by the model's lid. The Rayleigh friction coefficient k_R grows exponentially with height as $k_R = 2.7 \times 10^{-9} \exp(z/10^{-4})$, where z is the log-pressure height in meters. The characteristic damping time of the Rayleigh friction, $1/k_R$, reaches 1/18 sol near the top of the model at $\approx 5.31 \times 10^{-5}$ mbar.

2.6. Surface energy budget

A slab model is used to determine the evolution of the surface temperature (e.g., Gierasch and Goody, 1968; Zhang et al., 1982). The surface energy equation considers the balance between the net radiative flux of the solar and thermal components, the sensible heat flux from the surface to the atmosphere, and the heat flux into the soil. The thermal capacity of the soil is used to calculate the evolution of the surface temperature. The former is related to the thermal inertia. We use the thermal inertia map (Mellon et al., 2000) measured by the Thermal Emission Spectrometer on board the Mars Global Surveyor (TES–MGS). The net radiative flux on the surface is taken from the radiation schemes described above. The heat flux into the ground is modeled as in Zhang et al. (1982). The sensible heat flux into the atmosphere due to both the molecular conduction and turbulent diffusion is parameterized after Gierasch and Goody (1968). The latent heat flux is neglected in the present formulation.

2.7. CO_2 condensation and sublimation

Only thermal effects of CO_2 condensation and sublimation are considered in the model. Haberle et al. (1993) indicated that the change of mass of the martian atmosphere affects little the zonal mean circulation. When the predicted temperature of the air or surface drops below the freezing point, condensation of CO_2 occurs. The latent heat release is assumed to keep the temperature from falling below. Sublimation is the reverse process: it maintains the freezing temperature if the ice is heated. The condensation temperature of the CO_2 is calculated from the Clausius–Clapeyron relation (Hourdin et al., 1995). Mass effect of the atmospheric CO_2 condensation is ignored in this version of the model.

3. Results of simulations

3.1. Experiment design

To exclude the influence of the dust radiative effects and the uncertainty related to the dust load, spatial distribution, parameters of aerosol particles, we considered only the dustless $L_s = 90$ season. In all the numerical experiments we are to describe below, the model was spun up from the state of rest and the globally uniform temperature $T = 160$ K. The spin-up was performed for the perpetual Northern summer corresponding to the fixed solar longitude $L_s = 90°$. After 15 days of the integration time, the simulated fields achieve a quasi-steady state as determined from the total kinetic energy. If not otherwise explicitly stated, the diurnal solar cycle was used in the simulations. The results shown below represent snapshots at the end of the integration period. Since we use zonal average diagnostics, the results are almost equivalent to those obtained with daily averaged fields.

3.2. Control run with "full physics"

This simulation includes all the physics as described in the previous section. With the updates discussed above, it largely corresponds to the run presented by Hartogh et al. (2005). They demonstrated that the simulated zonally averaged temperature is in a good agreement with the TES–MGS nadir measurements (Smith et al., 2001) below ≈40 km for different seasons including the $L_s = 90°$ one. Recently, TES–MGS limb data up to ≈60 km became available (M. Smith, 2006, personal communication). The temperature data are scarce above 60 km and above 40 km in high latitudes. Therefore, at this point, we consider our results for the middle atmosphere as the "best guess" only.

The strong winter polar warming with the peak temperature of about 200 K around 60 km is seen in Fig. 1a. It is stronger than in some other martian GCMs, e.g., some GCMs show no warmings at all, others produce peak values ranging from 160 K (Forget et al., 1999) to 175 K (Kuroda et al., 2005). In line with other models, the minimum of temperature occurs in low latitudes. Between 60 and 70 km, this minimum is 5 to 15 K warmer than reported by Forget et al. (1999) and Moudden and McConnell (2005). To understand the reason of the latitude temperature contrast, we have plotted the zonally averaged net diabatic heating and cooling rates due to the absorption and thermal emission by CO_2 and dust in Fig. 1c. For comparison, the adiabatic heating and cooling due to the rising and sinking air is shown in Fig. 1d. The adiabatic heating/cooling rates are given as $\bar{Q}_{\rm ad} = -R\bar{w}^*\bar{T}/c_p H$ in the present formulation, where R is the gas constant, $\bar{w}^*$ is the residual vertical velocity, $\bar{T}$ is the zonal mean temperature, c_p is the heat capacity, and H is the scale height. It is seen, that the maximum of the diabatic cooling over the winter pole is around -30 K sol^{-1}, and coincides with the location of the polar temperature maximum. Contrary, the adiabatic heating in this area is 50 to 140 K sol^{-1}. In the low latitudes around 60 km, the diabatic and adiabatic heating rates are less than 10 and up to -35 K sol^{-1}, respectively. Therefore, the warming over the pole and the low latitude cold temperature are caused adiabatically by the corresponding downward and upward motions. Further we shall demonstrate how the strength of the meridional circulation is related to zonally asymmetric eddies (waves). As a measure of these eddies, we plotted root meat square (rms) zonal variations of the temperature in Fig. 1b. In the lower part of the model domain below

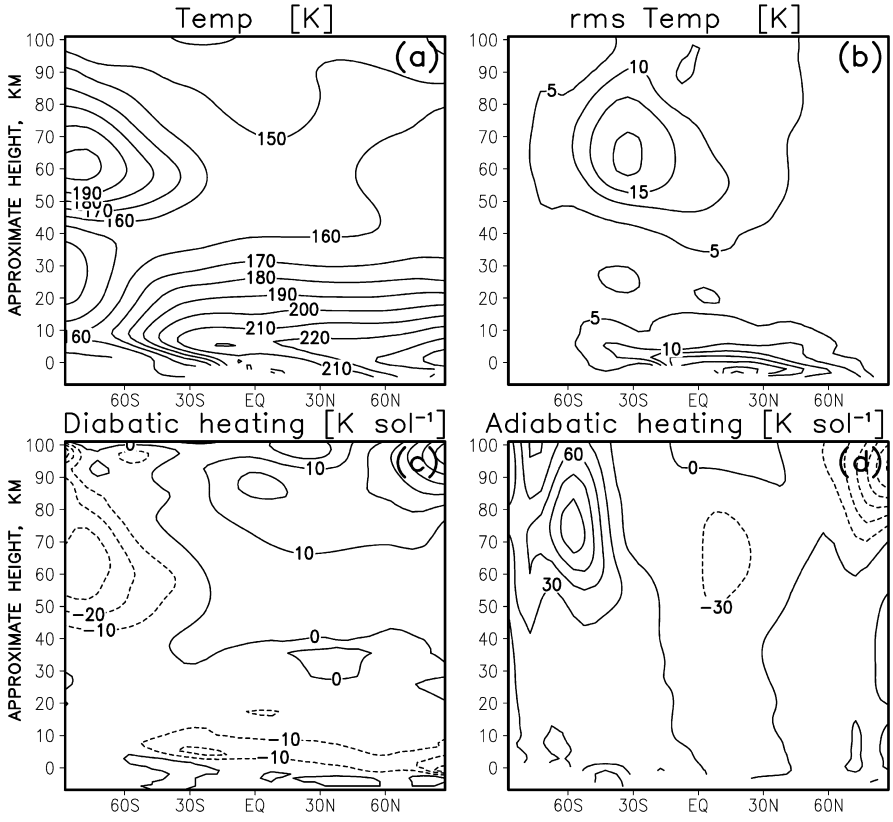

Fig. 1. Results of the run including the full physics ($L_s = 90°$): (a) zonal mean temperature; (b) rms longitudinal temperature variations; (c) diabatic heating/cooling rate; (d) adiabatic heating/cooling rate.

10 km, the strong rms fluctuations are due to planetary waves generated by the flow over the topography, and due to tides excited by the diurnal variations of the surface temperature. These eddies selectively propagate upward in accordance with the refractive properties of the atmosphere, and their magnitude grows as the air density decreases. The maximum of the longitudinal disturbances is seen between 60 and 70 km in Fig. 1b, where the rms temperature fluctuations peak at slightly more than 20 K in the southern hemisphere. Dissipative effects of the sponge layer are responsible for the decrease of fluctuations near the model lid.

The effect of eddies on the circulation enters the mean zonal momentum equation in the Transformed Eulerian Mean (TEM) formulation through the divergence of the Eliassen–Palm (EP) fluxes (Andrews et al., 1987):

$$\bar{u}_t + \bar{v}^*\left[(a\cos\phi)^{-1}(\bar{u}\cos\phi)_\phi - f\right] + \bar{w}^*\bar{u}_z = (\rho_0 a\cos\phi)^{-1}\nabla\cdot\mathbf{F} + a_{GW} - k_R\bar{u}. \quad (5)$$

In (5), overbars denote longitudinal averages, $\bar{v}^*$ and $\bar{w}^*$ are the residual velocities defined as $\bar{v}^* = \bar{v} - \rho_0^{-1}(\rho_0\overline{v'\theta'}/\bar{\theta}_z)_z$ and $\bar{w}^* = \bar{w} + (a\cos\phi)^{-1}(\cos\phi\overline{v'\theta'}/\bar{\theta}_z)_\phi$; ϕ is the latitude, $\theta = T\exp(Rz/c_pH)$ is the potential temperature, T is the temperature, f is the Coriolis parameter, $\mathbf{F}$ is the EP flux or wave action flux, a_{GW} is the parameterized drag due to subgrid-scale gravity waves, and k_R is the Rayleigh friction coefficient as described in Section 2.5. The residual circulation $(\bar{v}^*, \bar{w}^*)$ closely represents the meridional potential temperature transport. The corresponding stream lines are plotted in Fig. 2a. Two asymmetric poleward cells are seen below ≈70 km, and the pole-to-pole transport is above. Fig. 2b shows the meridional component of the residual velocity, $\bar{v}^*$, which varies from −35 to 5 m s^{-1}. Note that these values are several times larger than in the terrestrial middle atmosphere. For the perpetual $L_s = 90°$ season, the transience can be neglected in (5), $\bar{u}_t = 0$, and, to the accuracy of the advective terms, the meridional velocity can be determined as $\bar{v}^* \approx -(f\rho_0 a\cos\phi)^{-1}\nabla\cdot\mathbf{F} - f^{-1}a_{GW} + f^{-1}k_R\bar{u}$. Figs. 2c and 2d present the estimates of $\bar{v}^*$ calculated from the first two and the last terms of the latter equation. The contribution of the Rayleigh friction to the meridional velocity (up to −14 m s^{-1}) is negligible compared to the total $\bar{v}^*$ (Fig. 2b), at least below 80–90 km. This means that the sponge layer produces little distortions to the simulated fields in the run with the "full physics" below this height. As we shall see from our other numerical runs, this is not always the case. Gravity wave drag contributes about 10% of the EP flux divergence due to resolved eddies, mostly in the upper winter hemisphere. A closer examination of Figs. 2b and 2d reveals (see also Fig. 7 of Hartogh et al., 2005) that the velocity induced by the EP flux divergence (up to −20 m s^{-1}) provides a major contribution to the total $\bar{v}^*$ (up to −35 m s^{-1}). The visible exception between 60 and 90 km in the southern hemisphere denotes the area where the missing non-linear advection terms in (5) are important. In other words, the meridional transport is forced primarily by the eddies, and the strength of the eddies, or more precisely, of the corresponding EP flux divergence, determines the magnitude

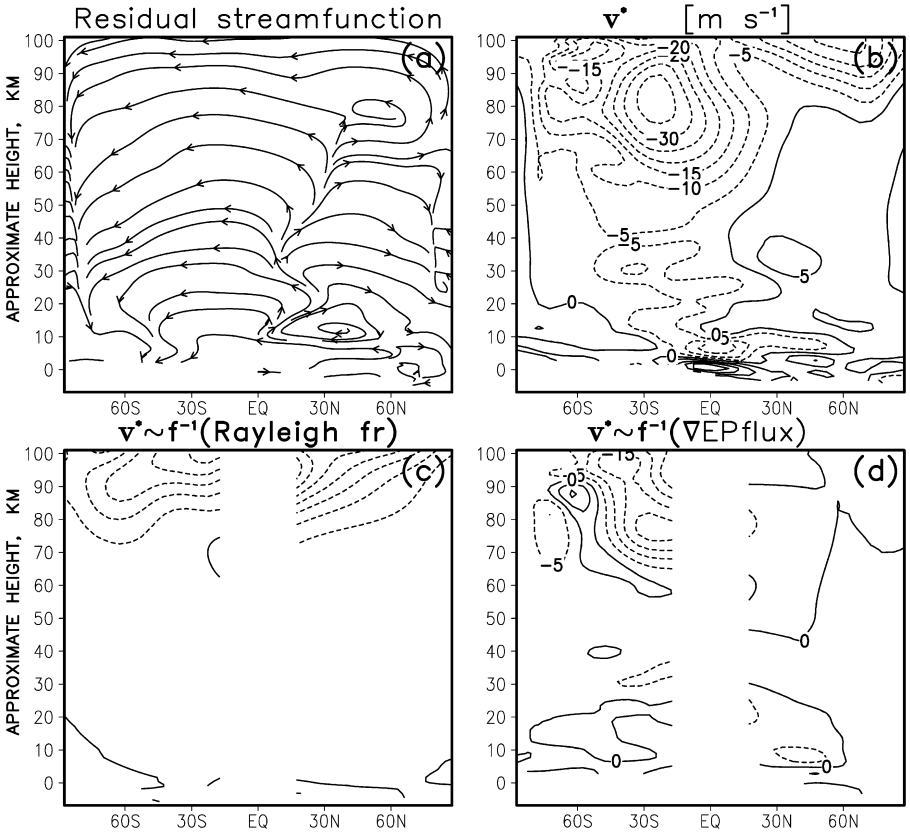

Fig. 2. Results of the run with the full physics: (a) stream lines of the residual circulation; (b) meridional residual velocity, $\bar{v}^*$; (c) estimate of the meridional residual velocity induced by the Rayleigh friction near the top of the model (the contour interval is 2 m s^{-1}); (d) estimate of the meridional residual velocity forced by the EP flux divergence (the contour interval is 10 m s^{-1}).

of the adiabatic heating or cooling and, ultimately, the degree of the winter polar warming.

3.3. Run with inhibited eddies

To demonstrate the above conclusion, we devised a sensitivity test with artificially reduced eddies. Under this scenario, a strong non-zonal Newtonian cooling of the form $T_t \sim -\alpha(z)(T - \bar{T})$ was added to the thermodynamic equation. This cooling affects only the deviations from the zonal mean by reducing the magnitudes of the disturbances $(T - \bar{T})$ and, thus, pushing the temperature towards the zonally averaged values $\bar{T}$. Presumably, the "non-zonal" cooling does not directly affect the mean circulation itself. The exponentially increasing with height coefficient $\alpha(z) = 2.25 \times 10^{-5} \exp(z/40\ [\text{km}])\ \text{s}^{-1}$ was used in this simulation. This corresponds to the characteristic damping time exponentially decaying from 1/9 to 1/34 sol near the model lid.

The simulated mean temperature and the rms deviations from the zonal mean are shown in Figs. 3a and 3b, respectively. The magnitude of the eddies is reduced by approximately a factor 4 compared to the control run of the previous subsection. The corresponding EP flux divergences are even weaker by factors 5–6. The temperature changed little (3–5 K colder) below ≈30 km in the southern hemisphere, and below ≈40 km in the northern one. The major differences with the "full physics" run occur above 30 km in the southern high latitudes. One feature that immediately stands out is the polar warming which is 20 K colder and shifted upward by about 10 km. This translates into the polar temperature at 50 km being 27 K cooler, and 7 K warmer near the top of the shown domain. In the high northern latitudes, the model generates slightly warmer (+3 K) temperatures above 60 km. The corresponding changes in diabatic heating/cooling rates (Fig. 2c) reflect the changes in the temperature field. Maximum of the cooling due to the CO_2 (up to -80 K sol^{-1}) above 90 km over the winter pole is shifted higher following the shift of the temperature maximum, and is 10 K sol^{-1} weaker at 60 km. The net diabatic cooling/heating rates outside the high altitude winter polar region have changed little. The adiabatic heating/cooling rates are plotted in Fig. 3d. Above 40 km, the adiabatic rates exceed the diabatic ones over the both poles, e.g., -50 vs 30 K sol^{-1} at 70 km over the South Pole, and 15 vs -100 K sol^{-1} at 80 km over the North Pole. The major change in the adiabatic cooling/heating rate distribution occurs in the high altitude winter hemisphere. There, the cooling rate weakened by almost 100 K sol^{-1} over 60° S (corresponds to weaker downward motions), and strengthened by 100 K sol^{-1} over the pole above 80 km (indicates stronger air descent). The corresponding residual stream function is plotted in Fig. 3d with the long dashed lines. It is seen that the circulation pattern is similar to the one in the "standard" simulation, however with the weaker equator-to-the-south-pole transport below 80 km: $\bar{v}^*$ up to only -20 m s^{-1} compared to -35 m s^{-1}

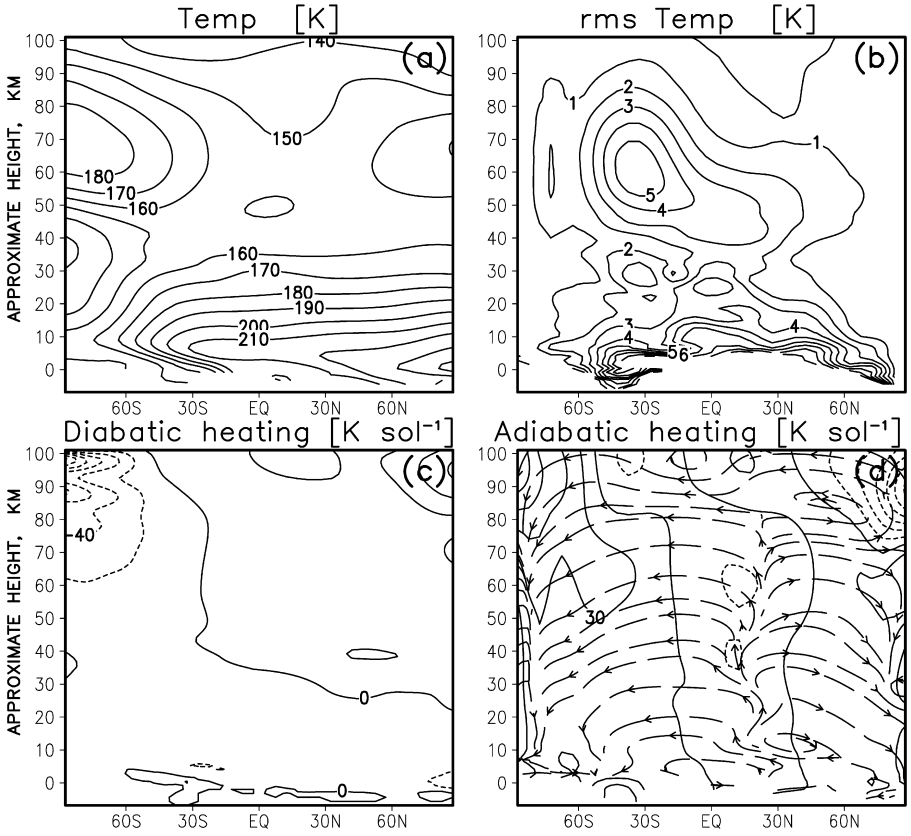

Fig. 3. Same as in Fig. 1 but for the run with the enhanced non-zonal Newtonian cooling to inhibit eddies in the model. On the panel (d), the contour interval for the adiabatic heating rate (solid lines) is 30 K sol^{-1}, and the stream lines of the residual circulation are shown with dashed arrow lines.

in the "standard" run. Comparison of the residual velocity $\bar{v}^*$ and its estimate from the EP flux divergence similar to the one in Figs. 2b–2d shows that, in midlatitudes below 50 km, the circulation is still driven primarily by the EP flux divergence due to the resolved eddies. Above 50 km, the circulation is influenced by the vertically increasing Rayleigh friction. Above 80 km, where the circulation demonstrates a pole-to-pole transport, the effect of the "sponge layer" dominates. In the upper Northern hemisphere, the gravity wave drag from the parameterized waves contributes almost as much as the resolved eddies.

As we saw above, the reduction of the strength of eddies in the model altered the meridional circulation and weakened the equator-to-pole transport in the winter hemisphere. As the result, the downward motions over the winter pole and the associated adiabatic warming reduced the polar temperature maximum. To emphasize the effects of eddies (or, more precisely, of their absence) on the meridional circulation, we ran the model under the scenario in which we significantly reduced the generation of planetary waves and tides in the model, rather than applying an extra damping to inhibit their propagation.

3.4. *Run with the flat topography and no diurnal variations*

A flow over the topography is known to be a strong source of planetary waves in atmospheres (Andrews et al., 1987). To reduce, or even remove altogether the excitation of these waves in the model, we assumed the flat martian topography by setting the surface elevations to zero. Furthermore, we prescribed the constant albedo (0.25) and thermal inertia (300 J m^{-2} K^{-1} s$^{-1/2}$) everywhere on the surface to get rid of the planetary wave excitation over the thermally inhomogeneous surface. We also turned off the solar diurnal cycle by replacing the time dependent solar heating rates with their daily averaged values. By doing so, we effectively removed the source of the solar tide in the model. Thus, the only eddies which remain in the simulation are those generated due to the instability and non-linearity of atmospheric motions.

The simulated zonal mean temperature and the rms deviations are shown in Figs. 4a and 4b, correspondingly. It is seen that the magnitude of eddy disturbances is reduced virtually to zero. As the result, the temperature field changed significantly both in the lower and upper atmosphere. The surface temperature is up to 35 K lower than in Fig. 1a, and the atmospheric temperature near the surface is from 35 K (in low latitudes) up to 60 K (over the summer pole) colder. Above 40 km, the air is up to 30 K warmer than in the "standard" run outside of the winter pole, and up to 30 K colder over it. The temperature in the winter polar maximum is almost the same as in the run with inhibited eddies. The other differences with that run are the colder lower atmosphere, and warmer air over the low latitudes above approximately 50 km.

The distribution of the diabatic heating in Fig. 4c reflects the simulated temperature field. It shows the net cooling in the

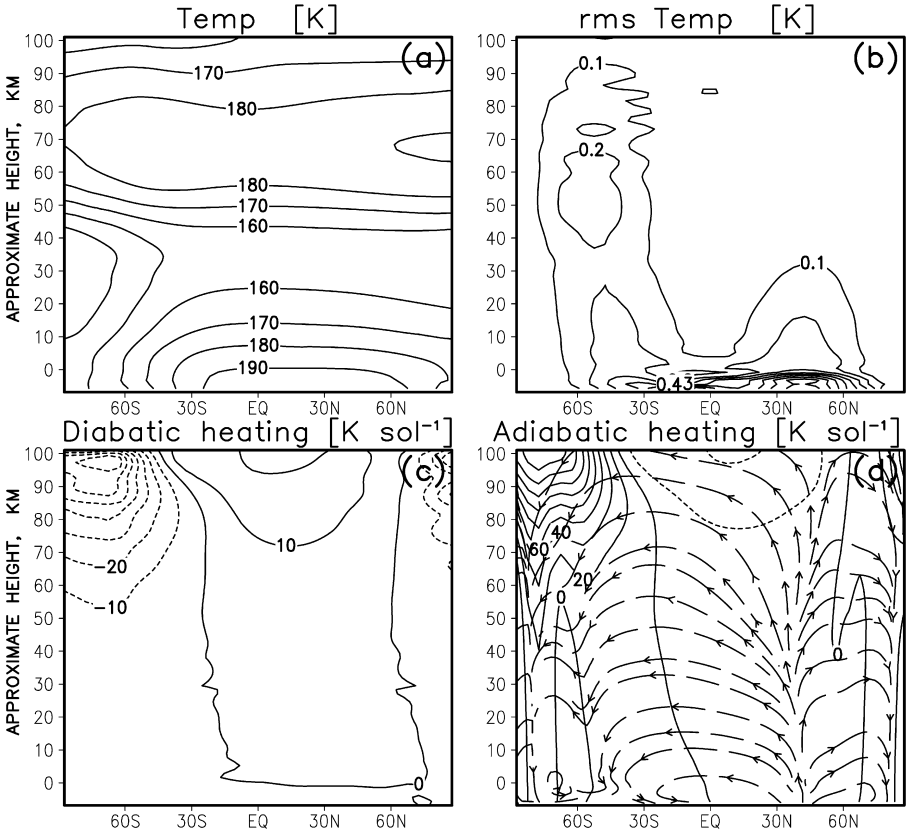

Fig. 4. Same as in Fig. 1 but for the run with the topography and diurnal solar cycle turned off to inhibit the generation of eddies in the model. Stream lines of the residual circulation are superimposed on the panel (d).

winter hemisphere, and the net heating in the summer one except in high latitudes. The cooling in the lower atmosphere is much weaker because of the colder temperature below 40 km. The adiabatic heating rate distribution in Fig. 4d has a reversed pattern: the net heating of up to 140 K sol^{-1} in the winter hemisphere, cooling of up to -40 K sol^{-1} in the summer one, and heating up to 40 K sol^{-1} over the summer pole. As in the previous simulations, the adiabatic heating exceeds the diabatic cooling in the winter polar mesosphere, although not as much as in the control run. Again, this fact demonstrates that the winter polar warming is caused dynamically by the downward flow. The residual circulation is plotted in the same figure with long dashed lines. It shows a two-cell pattern extended into the upper atmosphere. The imposed Rayleigh friction is practically the sole source of the meridional torque, which drives the circulation. Note, that the sponge layer was introduced to mimic missing damping effects of the molecular viscosity and non-orographic gravity waves, and to maintain the stability of the model. The meridional velocity is significantly weaker than in the runs described in the previous subsections (around $\bar{v}^* = 2$ m s^{-1} at 70 km), but increases exponentially following the Rayleigh friction. The simulated circulation pattern is similar to the direct thermally-induced nearly inviscid Hadley cells (Schneider, 2006, 1977) extended into the upper atmosphere. Note that on Earth, the Hadley circulation is confined to low latitudes, and is maintained by the surface drag and equatorial waves. In the simulation, these cells are driven by the Rayleigh friction drag.

The comparison of the sensitivity tests in Sections 3.3 and 3.4 with the control run demonstrated the important role of eddies in maintaining the residual meridional circulation in the martian middle atmosphere. The experiment described in the next subsection was designed to highlight the effects of the diabatic heating on the meridional circulation and, therefore, on the winter polar warming. Wilson (1997) reported on the simulation in which the increased heating during the global dust storm allowed the GCM to reproduce the warming phenomenon in the northern polar atmosphere during the $L_s = 270°$ season.

3.5. Run with the increased dust load

This numerical experiment is similar to the "full physics" run of Section 3.2 except for the dust opacity increased tenfold. As was mentioned earlier, the $L_s = 90°$ solstice is a relatively dustless season with the tropical dust optical depths in infrared of around $\tau = 0.05$ (Liu et al., 2003), or at least less than 0.1 (Smith, 2004). In our simulation, the infrared dust optical depth is equal to 0.5. With the adopted dust parameters, this corresponds to the visible optical depth around $\tau = 1.8$. This amount of dust was observed during the northern winter ($L_s = 270°$) solstices (e.g., Smith, 2004), but not during the $L_s = 90°$ season. Note, that simulated under these unrealistic

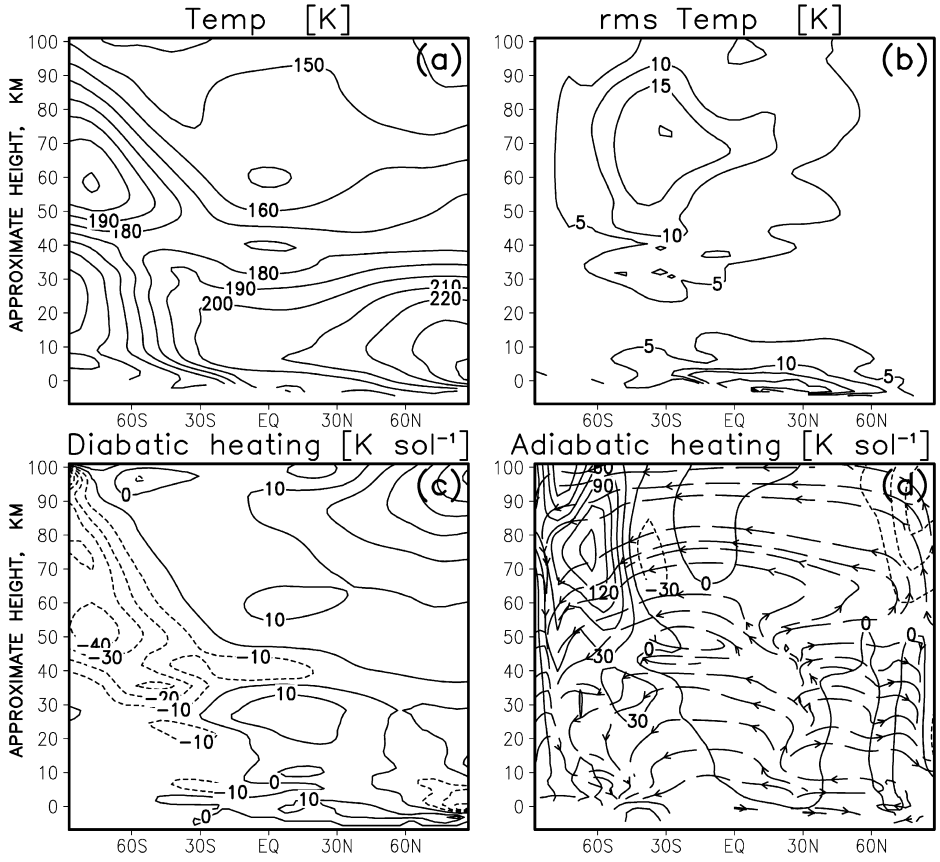

Fig. 5. Same as in Fig. 1 but for the run with the increased dust load. Stream lines of the residual circulation are superimposed on the panel (d).

(for $L_s = 90°$) conditions, fields are in no way expected to be close to observations, as was with the sensitivity tests reported on above.

The simulated temperature is consistent with the expectations for dust effects on Mars (Fig. 5a): the colder surface and the near surface atmosphere (up to −25 K over high summer latitudes), and the warmer layers above. The maximum of the aerosol heating effect is seen over the North Pole at ≈25 km ($\Delta T = 35$ K). At the same time, the temperature around 60 km over the winter pole, where there is no direct solar light, is more than 20 K higher. The other noticeable changes in the upper part of the model domain are ≈10 K colder temperature in the summer hemisphere, and the warmer air at low latitudes. These changes could not arise due to direct diabatic effects of the dust. The rms non-zonal temperature deviations shown in Fig. 5b have about the same magnitude as in the control run. However, a closer inspection shows an important redistribution of the wave activity: increased eddy variations in the winter midlatitudes above 80 km (up to 4 K), and between 30 and 50 km (up to 6 K). These differences are the manifestation of the changes in the propagation of planetary waves and tides in the model. Due to the stronger westerly jet in the winter hemisphere, the atmospheric refraction causes the EP fluxes (not shown here) to be directed more vertically below 50–70 km, and then to turn steeper towards the South Pole. This results in the upward shift of the negative EP flux divergences in the southern high latitudes.

The net diabatic heating/cooling rates are plotted in Fig. 5c. The contribution of the dust (not shown here) peaks at 45 K sol^{-1} in the northern hemisphere at 15–20 km, and is practically negligible to the south of 60° N. The −40 K sol^{-1} CO_2 net cooling over the winter pole is entirely due to the polar temperature maximum. The adiabatic heating/cooling rates and the stream lines of the residual circulation are shown in Fig. 5d. Qualitatively they are similar to those from the control run. The major difference is the stronger downward velocity (and the corresponding adiabatic heating) over the South Pole above ≈40 km.

4. Discussion

The numerical experiments reported above were designed to demonstrate the sensitivity of the meridional circulation to the mechanical (eddy) and diabatic (radiative) forcing. The problem we wanted to tackle with these tests is the nature of the solstitial transport in the martian atmosphere. The underlying question is whether the circulation is consistent with the thermally driven nearly inviscid Hadley cell (Schneider, 1977, 2006), or is it forced primarily by zonally asymmetric eddies (planetary and gravity waves, tides) via the "extratropical pump" mechanism (Holton et al., 1995), as in the terrestrial middle atmosphere? The temperature inversions and the corresponding warmings over the winter pole are caused adiabatically by the descending motions of the air, and, therefore, are

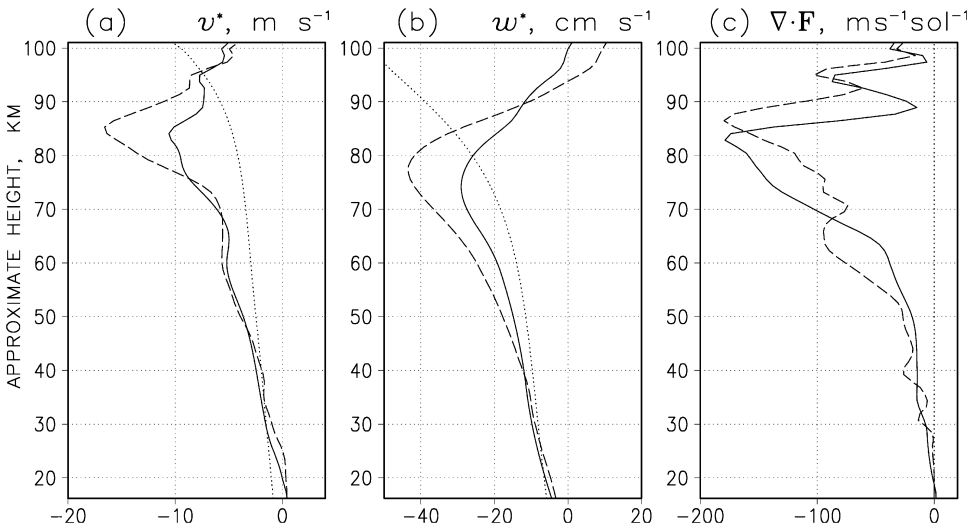

Fig. 6. Vertical profiles of the (a) meridional residual velocity, $\bar{v}$, (b) vertical residual velocity, $\bar{w}^*$, and (c) Eliassen–Palm flux divergence taken at 77.5° S. Solid lines are for the control run, dashed lines are for the run with the artificially increased dust load, and dotted lines are for the run with the flat topography and no diurnal variations.

the indications of how far poleward the meridional circulation cell extends.

All four experiments show the winter polar warmings. However, their location and strength are different. In the absence of eddies (Section 3.4), the meridional extent of the residual circulation is the smallest, its magnitude is the weakest, and the temperature maximum over the South Pole is the coldest and shifted up compared to the control run. Two "thermally direct" cells plotted in Fig. 4 extend all the way up to the model lid: rising air over the sub-solar latitude at 30° N, the smaller clockwise cell, and the larger counter-clockwise cell still confined to low latitudes. This pattern is consistent with the near inviscid circulation, which can be induced in the presence of a strong latitudinal temperature gradient (Schneider, 1977, 1983). Of course, mechanical effects like the inertial force and the surface friction are still required to maintain the circulation of this kind. In the upper part of the model domain, the pole-to-pole transport is induced entirely by the Rayleigh friction (sponge layer) introduced to the model to imitate the missing dissipative effects in the upper atmosphere.

The other three more realistic (in the sense that the eddies were included) experiments display a significant mechanical forcing of the meridional circulation. In the southern hemisphere, the meridional cell extends poleward in the middle atmosphere. An interesting aspect is the counter-clockwise meridional pole-to-pole transport in the middle atmosphere. Its existence inversely depends on the strength of eddies (or more precisely, on the magnitude of the associated EP flux divergence).

In all the experiments, strong EP flux divergences due to resolved eddies are located in high latitudes of the winter hemisphere near the upper edge of the westerly jet. Fig. 6 illustrates the relation between the mechanical forcing, $\nabla\cdot\mathbf{F}$, and the components of the residual velocity, $\bar{v}^*$ and $\bar{w}^*$. There, the vertical profiles of the above quantities at 77.5° S are plotted for the three experiments described in Sections 3.2, 3.4 and 3.5. As follows from Fig. 6c, $\nabla\cdot\mathbf{F} < 0$ in this area, has about the same magnitude in the "standard" and the "dust storm" runs, and virtually is zero in the experiment with no topography and tides. Note, that the direct radiative effects of the dust are negligible at this latitude, and the enhanced poleward torque is created by the dissipating eddies traveled from below and from low latitudes. As follows from Eq. (5), the meridional velocity $\bar{v}^*$ is locally proportional to the EP flux divergence (scaled by the density ρ_0), while the vertical velocity $\bar{w}^*$ integrally depends on $\nabla\cdot\mathbf{F}$ above according to the downward control principle (Holton et al., 1995). It is seen that $\bar{v}^*$ and $\bar{w}^*$ in Figs. 6a and 6b are, to a large degree, proportional to the mechanical forcing. In turn, the magnitude and location of the winter polar temperature maximum is determined by the adiabatic heating $\bar{Q}_{\rm ad} = -\bar{w}^* R\bar{T}/(c_p H)$.

The warmer polar temperature maximum in the run with the imposed "dust storm" is directly related to the upward shift of the area of strong wave breaking. Note, that $\nabla\cdot\mathbf{F}$ of the same magnitude but located higher produces stronger meridional torque because of the lower air density. The increase of the EP flux divergence in the high latitude winter middle atmosphere is achieved through a redirection of the wave action fluxes. A detailed consideration of this effect is beyond the scope of our paper, however, in outline, this mechanism is as follows. The strengthened winter polar jet (a prograde wind) modifies the refractive index for large scale planetary waves and the solar tide generated near the surface. As the result, waves are less likely to travel to high latitudes and to break there below 50 km. Instead, they are refracted somewhat higher (EP fluxes are directed more vertically), turn poleward, and, ultimately, break/dissipate near the upper edge of the winter polar vortex.

The atmosphere above 80 km is extremely sensitive in the presented numerical tests: even the direction of the transport changes sign from experiment to experiment. This uncertainty may point out to omitted effects, in particular those of grav-

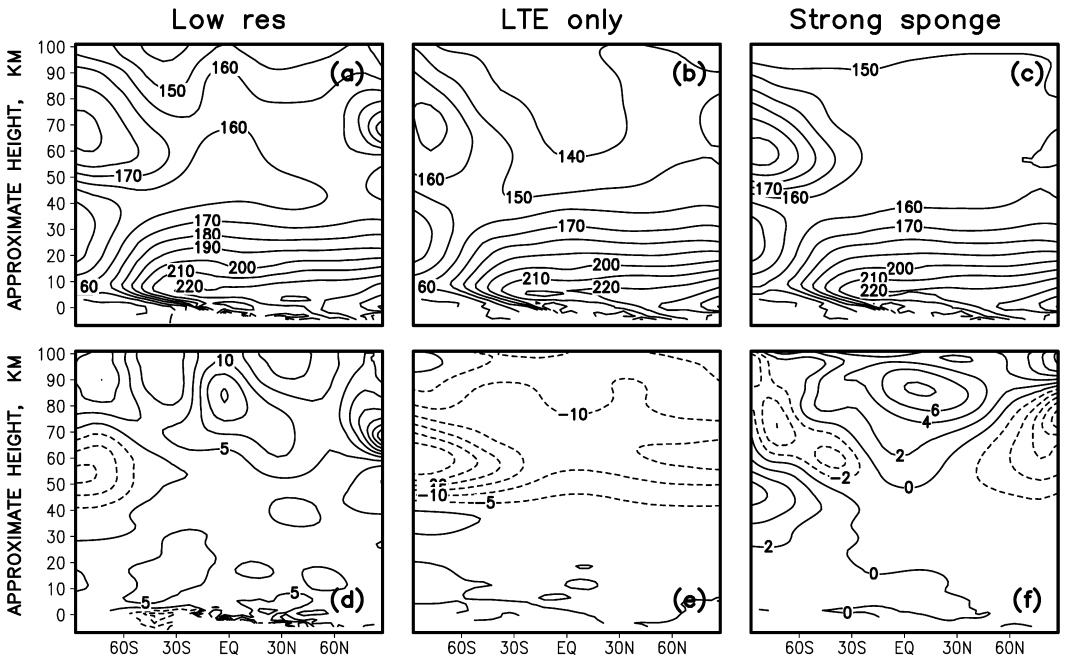

Fig. 7. Simulated temperature (first row) and the temperature difference with the "standard" run (second row) for 3 sensitivity experiments: (a) and (d) "low resolution" run with the number of longitudinal points reduced by factor 2; (b) and (e) the non-LTE scheme replaced by the LTE parameterization; (c) and (f) run with the sponge layer increased by factor 3.

ity waves (GW) generated by sources other than a flow over the topography. The first indication of such sources in the atmosphere of Mars was recently obtained from the MGS radio occultation measurements (Creasey et al., 2006). Normally, these waves have non-zero (with respect to the surface) phase velocities, can propagate higher, exert a drag on the mean flow and affect the circulation in the upper atmosphere. In all our runs, except perhaps in the run with no eddies, the EP flux divergence due to resolved waves exceeded the effect of parameterized GW almost by a factor 10. It is known that broad spectrum GW play a major role in driving the pole-to-pole circulation in the middle atmosphere of Earth. The atmosphere of Mars is, in general, convectively stable, therefore GWs of different phase velocities can exist. Instabilities in the lower atmosphere can provide an ample source of these waves. If included in martian GCMs, "non-orographic" GW can significantly alter the results in the upper atmosphere. To date, a lack of observational data does not allow to adequately constrain neither GW sources, nor zonally averaged fields. As the result of this uncertainty, definite conclusions about the circulation in the upper part of the model domain cannot be drawn in this study. In this context, it is important to discuss how possible changes in the simulated fields may affect the circulation below. First, the downward effect of the forcing decays exponentially (Holton et al., 1995). Therefore, one can expect that the possible effect of the broad-spectrum GW drag will be somewhat limited at the heights where winter polar warmings occur. Second, possibly stronger mechanical forcing due to GW would only enhance the conclusion that the circulation in the martian middle atmosphere is driven primarily by eddies, as on Earth.

5. Other factors that can affect polar warmings in GCM

Despite the good agreement of our simulations below 40 km with TES measurements and other martian GCMs (Hartogh et al., 2005), the polar warming of 200 K in the middle atmosphere in Fig. 1 appears to be stronger than in other models. For comparable dust conditions, other models generate peak values up to 175 K or lower, and some do not show warmings at all (J. Wilson, 2006, Martian Atmosphere Modeling Workshop, private communication). Given the absence of direct observations at these heights, it is, perhaps, prematurely to argue to what extent the value in Fig. 1 is realistic. Discussing reasons for this discrepancy with other models requires detailed intercomparisons, and is beyond the scope of this paper. Instead, we present 3 additional sensitivity tests demonstrating the degree of vulnerability of the simulated polar warming to variations of the model parameters.

The first experiment is the repeat of our "standard" run with the number of longitude grid points decreased by factor 2, i.e., to 16. Of course, resolution of this kind is barely used in contemporary GCMs. We chose it in order to magnify the effect of the low model resolution on the value of the temperature maximum. The latter is seen decreased by 10–190 K and shifted upward in Fig. 7a. This occurs due to the combination of more than 15 K colder air centered between 50 and 60 km, and 10 K warmer temperature at 90 km. The rms temperature variations in this run do not exceed 6 K, and are composed mostly of quasi-stationary waves with the zonal wave number 1. The amplitude of the semidiurnal tide is limited by 1.5 K at 70 km. Obviously, the reduced resolution does not allow proper representation of eddies in the model. Because of that, the EP flux divergence is weaker than in the "standard" run, the westerly jet

is stronger, has no meridional tilt, and is closed up exclusively by the Rayleigh friction. To some degree, the fields produced in the winter hemisphere are reminiscent of those in the run with artificially reduced eddies.

In the second experiment presented in Figs. 7b and 7e, we turned off the non-LTE cooling scheme for 15 μm CO_2 band in the upper atmosphere, and used the cooling rates from the LTE parameterization in the entire domain. This experiment is more realistic than the previous one in the sense that many martian GCMs employ LTE radiation schemes that do not account for the breakdown of the local thermodynamic equilibrium (non-LTE). Since LTE calculations tend to overestimate infrared cooling rates, the latters would tend to depress eddies stronger. Indeed, the rms temperature fluctuations are reduced in this run to 16 K. The polar temperature maximum decreases to 170 K, which is in line with other models (e.g., Kuroda et al., 2005). The net diabatic cooling rate in the winter hemisphere increased to -50 versus $-30\ \mathrm{K\,sol^{-1}}$ in the "standard" run. Consistently with the expectations about an LTE scheme, the diabatic heating got weaker (90 vs 140 $\mathrm{K\,sol^{-1}}$ in Fig. 1). However, it still exceeds the diabatic cooling, and, thus, determines the polar temperature maximum.

Dissipative properties of different dynamical cores of GCMs may also affect the simulated eddies. Implicit time integration schemes (with enhanced numerical dissipation) are often employed in circulation models in order to increase time steps (e.g., Moudden and McConnell, 2005, Section 2.1). It is very difficult to imitate the numerical dissipation delivered by different dynamical solvers. In our third sensitivity test, we simply increased the Rayleigh friction by factor 3 in expectation that it should crudely approximate stronger dissipation in the model. Effects of the enhanced sponge layer are mostly seen in the upper part of the model domain (Figs. 7c and 7d), and, in particular, over the winter pole. The simulated temperature is up to 6 K warmer below 50 km, and up to 6 K colder above. More specific conclusions, besides that the moderate variations of the numerical dissipation can modify the simulated temperature over the winter pole by several K, should probably not be drawn from this experiment given the very crude approximation.

The results presented in the paper may point out to a general reason for the discrepancies in simulations: the under/overestimation of eddies by a model can cause weaker/stronger polar warming. An indication to this effect is given by Forget et al. (1999). They explained the differences in the poleward extent of the meridional cell and the related strength of the warming between LMD and AOPP martian GCMs (with essentially the same physics) by different abilities of the models' dynamical cores to resolve eddy-mean flow interactions. Smoothed topography (Hartogh et al., 2005), too low model lid (Barnes and Haberle, 1996; Forget et al., 1999) can decrease the strength of the simulated polar warmings as well. More data on the zonal mean field are required to constrain models above 50–60 km.

6. Conclusions

We present a series of numerical experiments with a recently developed general circulation model of the martian atmosphere (Hartogh et al., 2005) to examine the role of the mechanical and diabatic forcing on the meridional circulation. The strength and the poleward extent of this circulation, rather than the direct radiative heating effects, determine the magnitude and the location of the winter polar warmings observed in the atmosphere of Mars. Partly, this work was motivated by findings that onsets of global dust storms enhance the winter polar temperature maximums. In this regard, it is important to answer the question if the meridional circulation in the middle atmosphere of Mars is consistent with the thermally driven almost inviscid Hadley cell, as argued by Wilson (1997) and Forget et al. (1999), or it primarily is driven by eddies (planetary and gravity waves, solar tide) similarly to the so-called "extratropical pump" mechanism (Holton et al., 1995), as on Earth.

Four sensitivity tests were described in this paper: the control run, the one with the artificial damping of non-zonal disturbances, the experiment with no topography and diurnally averaged solar heating to inhibit the generation of eddies, and the run with the increased dust load imitating a global dust storm. In all but the experiment with no planetary waves and tides (weak planetary waves generated by instabilities were still present), we found that the circulation is forced, to a large degree, by the mechanical effects of dissipating eddies. The strength and location of winter polar warmings are related to the divergence of wave action fluxes (Eliassen–Palm fluxes) in the manner consistent with the mechanism of the "extratropical pump," at least in the middle atmosphere. Only in the run with severely reduced eddies, the meridional transport was reminiscent of the thermally-induced Hadley cell. In agreement with earlier arguments of Haberle et al. (1982), this circulation was confined to low latitudes. The run with an increased dust revealed that the magnification of the winter polar warming is not the direct result of heating due to the increased absorption of the solar radiation by the aerosol, but is caused by the extension of the meridional transport cell poleward. This conclusion corroborates the result of Wilson (1997), although in his experiment the dust was allowed to be transported, and, thus, to potentially magnify the effect. A closer examination have shown the mechanism of the poleward extension of the meridional cell. Strengthened westerly polar jet (prograde winds) forces planetary waves and tides propagate more vertically, and preventing them from dissipating at lower levels. Then, the Eliassen–Palm fluxes converge stronger near the upper edge of the polar vortex, and magnify the poleward transport. Correspondingly, the air descent over the pole intensifies, and the temperature maximum increases as well.

Additional numerical experiments have shown that insufficient model resolution, increased numerical dissipation, and, especially, neglect of non-LTE effects for the 15 μm CO_2 band radiative cooling could weaken the simulated meridional transport, and, as the result, decrease the magnitude of winter polar warmings in GCMs.

High sensitivity of the circulation above ≈80 km may be an indication of missing effects in our and other contemporary GCMs. A potential candidate is the gravity wave drag exerted by broad-spectrum harmonics. Further measurements of large scale wind and temperature fields in the upper atmosphere as well as the statistics for small scale fluctuations will help to constrain the models and verify the nature of the meridional circulation.

Acknowledgments

This work was supported by Deutsche Forschungsgemeinschaft, Project HA 3261/1-2. We are grateful to M. Smith of NASA for providing us with the MGS–TES limb and nadir data, and for helpful comments.

References

Andrews, D.G., Holton, J.R., Leovy, C.B., 1987. Middle Atmosphere Dynamics. Academic Press, San Diego, CA.

Barnes, J.R., 1990. Possible effects of breaking gravity waves on the circulation of the middle atmosphere of Mars. J. Geophys. Res. 95 (B2), 1401–1421.

Barnes, J.R., Haberle, R.M., 1996. The martian zonal-mean circulation: Angular momentum and potential vorticity structure in GCM simulations. J. Atmos. Sci. 53, 3143–3156.

Barnes, J.R., Hollingsworth, J.L., 1987. Dynamical modeling of a planetary wave mechanism for a martian polar warming. Icarus 71 (2), 313–334.

Berger, U., von Zahn, U., 1999. The two-level structure of the mesopause: A model study. J. Geophys. Res. 104, 22083–22093.

Christensen, P.R., and 25 colleagues, 2001. Mars Global Surveyor Thermal Emission Spectrometer experiment: Investigation description and surface science results. J. Geophys. Res. 106, 23823–23872, doi:10.1029/2000JE001370.

Collins, M., Lewis, S.R., Read, P.L., 1997. Gravity wave drag in a global circulation model of the martian atmosphere: Parameterization and validation. Adv. Space Res. 19 (8), 1245–1254.

Creasey, J.E., Forbes, J.M., Hinson, D.P., 2006. Global and seasonal distribution of gravity wave activity in Mars' lower atmosphere derived from MGS radio occultation data. Geophys. Res. Lett. 33 (L01803), doi:10.1029/2005GL024037.

Delacourt, C., Gros, N., Allemand, P., Baratoux, D., 2003. Online Mars digital elevation model derived from MOLA profiles. Eos Trans. AGU 84 (52).

Deming, D., Mumma, M.J., Espenal, F., Kostiuk, T., Zipoy, D., 1986. Polar warming in the middle atmosphere of Mars. Icarus 66, 366–379.

Forget, F., Hourdin, F., Fournier, R., Hourdin, C., Talagrand, O., Collins, M., Lewis, S.R., Read, P.L., Huot, J.-P., 1999. Improved general circulation models of the martian atmosphere from the surface to above 80 km. J. Geophys. Res. 104, 24155–24175.

Gierasch, P., Goody, R., 1968. A study of the thermal and dynamical structure of the martian lower atmosphere. Planet. Space Sci. 16, 615–646.

Gusev, O.A., Kutepov, A.A., 2003. Non-LTE gas in planetary atmospheres. In: Hubeny, I., Mihalas, D., Werner, K. (Eds.), Stellar Atmosphere Modeling. In: ASP Conference Series, vol. 288, pp. 318–330.

Haberle, R.M., Leovy, C.B., Pollack, J.B., 1982. Some effects of global dust storms on the atmospheric circulation of Mars. Icarus 50, 322–367.

Haberle, R.M., Pollack, J.B., Barnes, J.R., Zurek, R.W., Leovy, C.B., Murphy, J.R., Lee, H., Schaeffer, J., 1993. Mars atmospheric dynamics as simulated by NASA Ames general circulation model. 1. The zonal-mean circulation. J. Geophys. Res. 98, 3093–3123.

Hartogh, P., Jarchow, C., Sonnemann, G.R., Grygalashvyly, M., 2004. On the spatiotemporal behavior of ozone within the upper mesosphere/mesopause region under nearly polar night conditions. J. Geophys. Res. 109 (D18303), doi:10.1029/2004JD004576.

Hartogh, P., Medvedev, A.S., Kuroda, T., Saito, R., Villanueva, G., Feofilov, A.G., Kutepov, A.A., Berger, U., 2005. Description and climatology of a new general circulation model of the martian atmosphere. J. Geophys. Res. 110 (E11008), doi:10.1029/2005JE002498.

Holton, J.R., Haynes, P.H., McIntyre, M.E., Douglass, A.R., Rood, R.E., Pfister, L., 1995. Stratosphere–troposphere exchange. Rev. Geophys. 33 (4), 403–439.

Holtslag, A.A.M., Boville, B.A., 1993. Local versus non-local boundary-layer diffusion in a global climate model. J. Climate 6, 1825–1842.

Hourdin, F., Forget, F., Talagrand, O., 1995. The sensitivity of the martian surface pressure and atmospheric mass budget to various parameters: A comparison between numerical simulations and Viking observations. J. Geophys. Res. 100, 5501–5523.

Jakosky, B.M., Martin, T.Z., 1987. Mars: North-polar atmospheric temperatures during dust storms. Icarus 72, 528–534.

Kuroda, T., Hashimoto, N., Sakai, D., Takahashi, M., 2005. Simulation of the martian atmosphere using a CCSR/NIES AGCM. J. Meteorol. Soc. Jpn. 83, 1–19.

Kutepov, A.A., Gusev, O.A., Ogibalov, V.P., 1998. Solution of the non-LTE problem for molecular gas in planetary atmospheres: Superiority of accelerated lambda iteration. J. Quant. Spectrosc. Radiat. Trans. 60, 199–220.

Liu, J., Richardson, M.I., Wilson, R.J., 2003. An assessment of the global, seasonal, and interannual spacecraft record of martian climate in the thermal infrared. J. Geophys. Res. 108, doi:10.1029/2002JE001921.

McFarlane, N.A., 1987. The effect of orographically excited gravity wave drag on the general circulation of the lower stratosphere and troposphere. J. Atmos. Sci. 44, 1775–1800.

Medvedev, A.S., Klaassen, G.P., 2000. Parameterization of gravity wave momentum deposition based on a non-linear theory of wave spectra. J. Atmos. Solar-Terr. Phys. 62, 1015–1033.

Mellon, M.T., Jakosky, B.M., Kieffer, H.H., Christensen, P.R., 2000. High resolution thermal inertia mapping from the Mars Global Surveyor Thermal Emission Spectrometer. Icarus 148, 437–455.

Mihalas, D., 1978. Stellar Atmospheres, second ed. Freeman, New York.

Moudden, Y., McConnell, J.C., 2005. A new model for multiscale modeling of the martian atmosphere, GM3. J. Geophys. Res. 110 (E04001), doi:10.1029/2004JE002354.

Nakajima, T., Tanaka, M., 1986. Matrix formulations for the transfer of solar radiation in a plane-parallel scattering atmosphere. J. Quant. Spectrosc. Radiat. Trans. 35, 13–21.

Nakajima, T., Tsukamoto, M., Tsushima, Y., Numaguti, A., Kimura, T., 2000. Modeling of the radiative processes in an atmospheric general circulation model. Appl. Opt. 39 (N27), 4869–4878.

Rothermel, H., Kaufl, H.U., Schrey, U., Drapatz, S., 1988. Thermal structure of the martian mesosphere. Astron. Astrophys. 196, 296–300.

Rybicki, G.B., Hummer, D.G., 1992. An accelerated lambda iteration method for multilevel radiative transfer. 2. Overlapping transitions with full continuum. Astron. Astrophys. 262, 209–215.

Santee, M., Crisp, D., 1993. Thermal structure and dust loading of the martian atmosphere during late southern summer—Mariner-9 revisited. J. Geophys. Res. 98 (E2), 3261–3279.

Schneider, E.K., 1977. Axially symmetric steady-state models of the basic state for instability and climate studies. Part II. Non-linear calculations. J. Atmos. Sci. 34, 280–296.

Schneider, E.K., 1983. Martian great dust storms: Interpretive axially symmetric models. Icarus 55, 302–331.

Schneider, T., 2006. The general circulation of the atmosphere. Annu. Rev. Earth Planet. Sci. 34, 655–688, doi:10.1146/annurev.earth.34.031405.125144.

Shapiro, R., 1970. Smoothing, filtering, and boundary effects. Rev. Geophys. Space Phys. 8, 359–387.

Smith, M.D., 2004. Interannual variability in TES atmospheric observations of Mars during 1999–2003. Icarus 167, 148–165.

Smith, M.D., Pearl, J.C., Conrath, B.J., Christensen, P.R., 2001. Thermal Emission Spectrometer results: Mars atmospheric thermal structure and aerosol distribution. J. Geophys. Res. 106, 23929–23945.

Takacs, L.L., Balgovind, R., 1983. High latitude filtering in global grid point models. Mon. Weather Rev. 111, 2005–2015.

Theodore, B., Lellouch, E., Chassefiere, E., Hauchecorne, A., 1993. Solstitial temperature inversions in the martian middle atmosphere: Observational clues and 2-D modeling. Icarus 105, 512–528.

Wilson, R.J., 1997. A general circulation model of the martian polar warming. Geophys. Res. Lett. 24, 123–126.

Zhang, D., Anthes, R.A., 1982. A high-resolution model of the planetary boundary layer-sensitivity tests and comparisons with SESAME-79 data. J. Appl. Meteorol. 21, 1594–1609.